


X-ray microtomosynthesis of unstained pathology tissue samples

David T. Nguyen¹ | Thomas C. Larsen² | Muyang Wang¹ | Russel H. Knutsen¹ | Zhihong Yang¹ | Eric E. Bennett¹ | Dumitru Mazilu¹ | Zu-Xi Yu¹ | Xi Tao³ | Danielle R. Donahue⁴ | Ahmed M. Gharib⁵ | Christopher K. E. Bleck¹  | Joel Moss¹ | Alan T. Remaley¹ | Beth A. Kozel¹ | Han Wen¹ 

¹ National Heart, Lung and Blood Institute, National Institutes of Health, Bethesda, Maryland

² College of Medicine, University of Arizona, Tucson, Arizona

³ School of Biomedical Engineering, Southern Medical University, Guangzhou, Guangdong, China

⁴ Mouse Imaging Facility, National Institutes of Health, Bethesda, Maryland

⁵ National Institute of Diabetes and Digestive and Kidney Diseases, National Institutes of Health, Bethesda, Maryland

Correspondence

Han Wen, National Heart, Lung and Blood Institute, National Institutes of Health, Building 10, Room B1D523, 10 Center Drive, MSC 1061, Bethesda, MD 20892, USA.

Email: wenh@nhlbi.nih.gov

Abstract

In pathology protocols, a tissue block, such as one containing a mouse brain or a biopsy sample from a patient, can produce several hundred thin sections. Substantial time may be required to analyse all sections. In cases of uncertainty regarding which sections to focus on, noninvasive scout imaging of intact blocks can help in guiding the pathology procedure. The scouting step is ideally done in a time window of minutes without special sample preparation that may interfere with the pathology procedures. The challenge is to obtain some visibility of unstained tissue structures at sub-10 μm resolution.

We explored a novel x-ray tomosynthesis method as a way to maximise contrast-to-noise ratio, a determinant of tissue visibility. It provided a z -stack of thousands of images at 7.3 μm resolution (10% contrast, half-period of 68.5 line pairs/mm), in scans of 5–15 minutes. When compared with micro-CT scans, the straight-line tomosynthesis scan did not need to rotate the sample, which allowed flat samples, such as paraffin blocks, to be kept as close as possible to the x-ray source. Thus, given the same hardware, scan time and resolution, this mode maximised the photon flux density through the sample, which helped in maximising the contrast-to-noise ratio. The tradeoff of tomosynthesis is incomplete 3D information.

The microtomosynthesis scanner has scanned 110 unstained human and animal tissue samples as part of their respective pathology protocols. In all cases, the z -stack of images showed tissue structures that guided sectioning or provided correlative structural information. We describe six examples that presented different levels of visibility of soft tissue structures. Additionally, in a set of coronary artery samples from an HIV patient donor, microtomosynthesis made a new dis-

covery of isolated focal calcification in the internal elastic lamina of coronary wall, which was the onset of medial calcific sclerosis in the arteries.

KEYWORDS

diffuse cystic lung disease, Mönckeberg sclerosis, paraffin-embedded tissue, straight-line microtomosynthesis, unstained tissue, vascular calcification, x-ray microscopy

1 | INTRODUCTION

Pathology protocols often generate hundreds of histology sections per tissue sample, and some research studies involve many samples from large cohorts of mice. Staining and analysing just a fraction of these sections becomes a laborious task. Similarly, clinical pathology test of biopsy specimen forces a trade-off between patient throughput and sampling density per sample.^{1–3} One approach to ease the problem is rapid scouting of intact tissue samples with a noninvasive imaging method to guide the sectioning and analysis to locations of interest.⁴ Ideally, the scouting step would be done in a window of minutes particularly in fresh biopsy samples. It should be able to provide a z-stack of cross-sectional images at $<10\ \mu\text{m}$ resolution and slice spacing (histology sections are typically $5\text{--}10\ \mu\text{m}$ thick), without special sample preparation or staining that might interfere with subsequent pathology procedures.

Laboratory microcomputed tomography (micro-CT) has been used extensively for noninvasive correlative studies that complement traditional pathology results (see Refs. 4–6 for a review of the vast literature). For rapid scouting of unstained samples, micro-CT results have been mixed.⁴ It performs extremely well in structures of large density variation, such as calcification deposits in tissue, dehydrated tissue,^{7,8} or prestained samples for electron microscopy.^{4,9} At the other end of the spectrum are low contrast samples, such as soft tissue samples immersed in water or a buffer solution, which can be difficult to see without lengthy scans.^{4,10} Phase-contrast methods have the potential to enhance visibility, but due to instrumentation requirements is not yet developed for rapid scouting at high resolution.⁴

Tissue visibility is limited by image contrast-to-noise ratio, which depends on the number of photons that illuminate each voxel over the duration of the scan. It scales inversely with the distance between the sample and the x-ray focal spot, given the same hardware and image resolution. In this regard, we explored a *tomographic method that allowed flat samples such as tissue in standard paraffin-embedding cassettes to be kept at a minimal distance from the x-ray focal spot, by removing the need to rotate the sample in the beam*. Referring to Figure 1, it is a tomosynthesis method¹¹ wherein the sample is scanned in a straight line

across a cone beam.^{12–15} Some aspects of the method were connected to the historical ‘planigraphy’ from an early era of film radiography.¹⁶ *With standard tissue-embedding cassettes, the minimal sample-to-focal spot distance is reduced by half relative to full CT scans, corresponding to double the contrast-to noise ratio at the same resolution and scan*

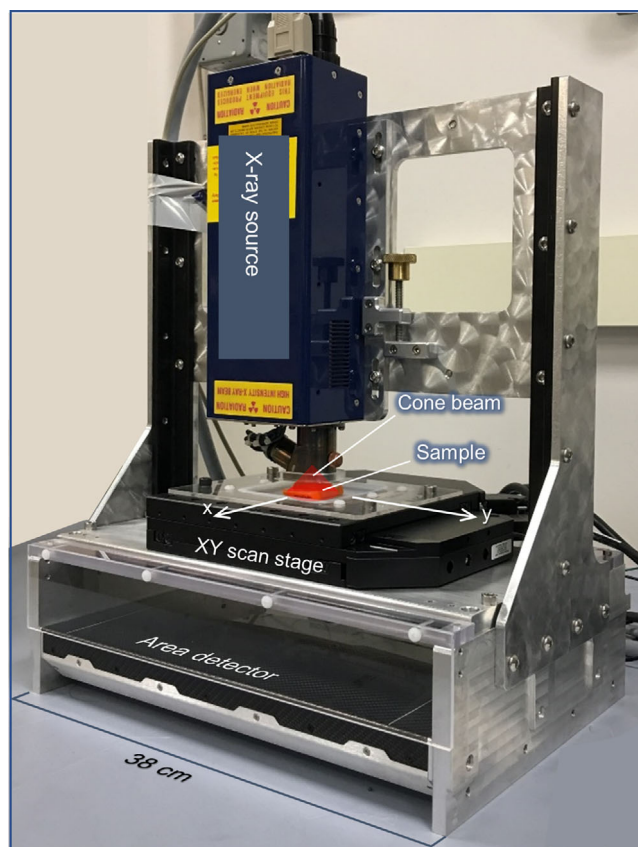


FIGURE 1 The x-ray straight-line tomosynthesis scanner without the radiation enclosure. The outer dimensions are 38 cm by 30 cm by 60 cm (height). The moving part of the system is the sample stage, which is motorised in the horizontal plane. The sample is scanned horizontally across the vertical cone beam, in the x or y direction. The projection of the cone beam provides a maximal $16.8\times$ geometric magnification. Given the same x-ray source and detector, this mode of scan allowed a flat sample to be kept as close as possible to the x-ray focal spot, thereby maximising the photon flux density through the sample and the geometric magnification for greater contrast-to-noise ratio and resolution. The tradeoff of tomosynthesis is incomplete 3D resolution when compared to a full CT scan

time. This type of scan also maximised the geometric magnification, which allowed the use of efficient flat panel detectors of fairly large pixels ($75\ \mu\text{m}$). Although straight-line tomosynthesis is used in security screening,^{14,17} to our knowledge, this is the first adaptation for microscopy of pathology samples.

The tradeoff in tomosynthesis when compared to full CT scans are anisotropic resolution where the in-plane resolution is higher than depth resolution, and incomplete 3D information. Tomosynthesis scans are often reconstructed into a z-stack, which is a stack of horizontal cross-sectional images of a small incremental spacing. Image reconstruction and limitations of tomosynthesis became well understood as clinical digital breast tomosynthesis became a standard of care.¹⁸ *For rapid scans of unstained samples at sub-10 μm resolution, we found in practice that the limiting factor was tissue structure visibility rather than 3D rendition when determining the slices that contain features of interest.*

Some 110 unstained tissue samples of various types have been scanned with this method, including²² human tissue samples. The samples were up to several centimetres in size and 1.5 cm in thickness. *While individual cells were not visible at 5-7 μm voxel size without contrast staining, most samples showed some recognisable tissue structures of interest at this scale.* We describe six examples of different levels of challenge, ranging from calcification deposits which were highly visible, to fresh tissue immersed in water which presented weak contrast. In human coronary artery samples, benchmark micro-CT scans on two commercial systems were also performed to verify the position of the cross-sectional slices from microtomosynthesis (see the 'Benchmark scans on two commercial micro-CT scanners' subsection of 'Materials and Methods' below for instrument details).

2 | MATERIALS AND METHODS

2.1 | Examples of sample handling and study procedure

To represent a range of difficulties in seeing tissue structures, we describe several examples. High contrast (easy) examples include a formalin-fixed paraffin-embedded (FFPE) block of coronary artery segments from an HIV patient donor, FFPE block of heart specimens from ApoE knock-out (ApoE^{-/-}) mice; medium contrast examples are FFPE blocks of mouse brain specimens and of lung parenchyma tissue specimens from patients with the cystic lung disease lymphangioleiomyomatosis (LAM); a low contrast situation is the soft tissue structure of fresh mouse aortas immersed in water. The study procedure for each example is described below.

2.1.1 | Coronary artery samples from an HIV patient donor

The overall aim of the pathology protocol was to understand the history of coronary artery disease in HIV.¹⁹ Left ascending coronary artery segments were processed into FFPE blocks with a Leica ASP-300 tissue processor (Figure 2A). Besides the tomosynthesis scan, benchmark micro-CT scans on two commercial systems were performed to verify the positions of the reconstructed cross-sections from microtomosynthesis. Visibility of tissue structures was measured by the contrast-to-noise ratio (CNR) between the arterial wall and the surrounding wax medium, taking the standard deviation of pixel values in featureless wax areas as the noise. Locations of interests were identified in 3D space from the tomosynthesis z-stack. The blocks were sectioned to those locations in 10 μm steps. Slices of 5-10 μm thickness were mounted in positively charged slides. The slides were stained with either haematoxylin and eosin (H&E), or von Kossa stain for detection of calcium phosphate deposits while also delineating the layers of the arterial wall. The slides were scanned in a Hamamatsu digital slide scanner (NanoZoomer Res 2.0, Shizuoka Pref., Japan).

2.1.2 | Lung parenchymal tissue specimen from a LAM patient

Patients with LAM develop diffused, air-filled cysts in their lungs, accompanied with decreased pulmonary function and diffusion.²⁰ The aim of the pathology study was the structure and cellular composition of the cyst wall. Parenchymal tissue was processed into FFPE blocks as described above (Figure 3A). The blocks were imaged to identify locations of cysts with intact walls, which guided sectioning to produce 5 μm thick slices. The slices were H&E stained and optically scanned. The cell types present in the cyst wall were recognised by their appearance with H&E staining.

2.1.3 | Mouse heart samples

The samples were from 1-year-old ApoE^{-/-} mice. The aim of the study was to image the distribution of calcification in the aortic root, and possible calcification deposits on the aortic valve. The samples were fixed and embedded in paraffin as described above. In the x-ray images, calcification deposits were visible by their strong x-ray absorption compared to the surrounding soft tissue. Quantitative mass distribution of calcification was measured with a modified single-energy x-ray absorptiometry method.²¹

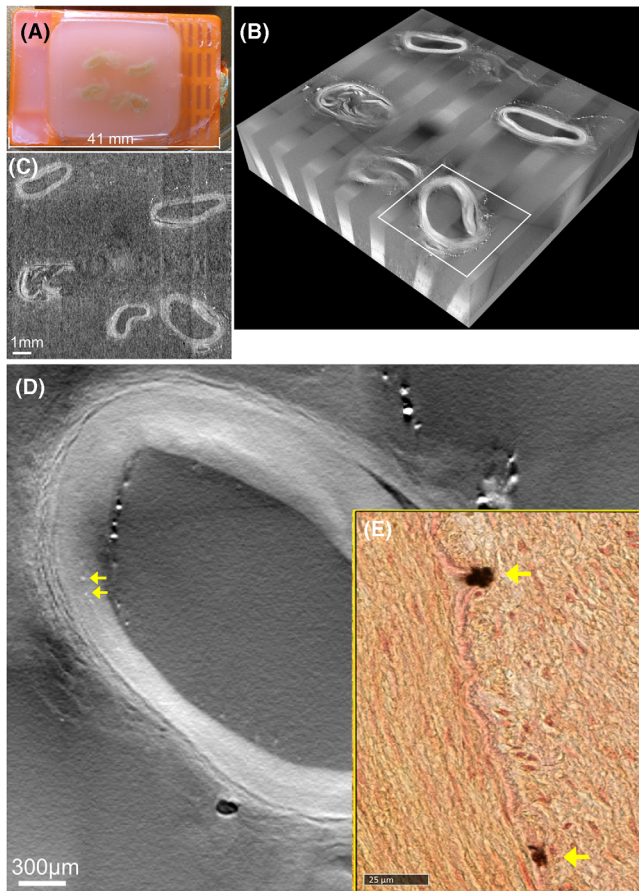


FIGURE 2 Tomosynthesis scan and histology of a paraffin block containing unstained coronary artery segments from an HIV patient donor. **(A)** A photo of the paraffin-embedded artery segments. **(B)** A cutaway of the reconstructed 3D volume from microtomosynthesis, exposing a top surface which was at a level of 1.9 mm below the surface of the paraffin block. The surface cuts across the 5 vessel segments. Vessel walls appear bright against the wax medium due to their higher x-ray attenuation. Out-of-plane shadows of the cassette grid at the bottom of the block can be seen. **(C)** A cross-section at the same depth from a reference benchmark micro-CT scan which verified the position of the tomosynthesis cross-section. The CT image voxel size was $30.5 \times 30.5 \times 60.9 \mu\text{m}^3$. **(D)** A magnified view of the artery segment outlined by the rectangle in panel B. Isolated bright dots between the intimal and medial layers are indicated by yellow arrows. **(E)** Histology section of the same location with Von Kossa staining. By matching the two types of images, the bright dots in the x-ray cross-section were identified as microcalcification in the internal elastic lamina of the arterial wall, which was recognised as the onset of medial calcific sclerosis associated with HIV

2.1.4 | Mouse brain sample

The brain specimen of an Eln+/- mouse was studied for possible vascular abnormalities arising from the genetic modification.²² The specimen underwent the fixation and paraffin-embedding process as described above. Starting from the tomosynthesis z-stack, cross-sectional images

along the curved paths of blood vessels were obtained using an in house custom-built software based on user-defined landmarks.

2.1.5 | Mouse aorta samples

X-ray imaging was used to quantify the total mass of calcification in atherosclerotic plaques within the aorta samples of 1-year-old ApoE-/- mice. The sample length was from the aortic arch to the common iliac arteries. The fresh aortas were lightly irrigated with 10% buffered formalin for several seconds for preservation without rubberising the tissue, underwent a tomosynthesis scan, then cut lengthwise and laid open to expose the lumen, stained with Sudan IV red for lipids, and sealed in phosphate-buffered saline (PBS) solution between two plastic microscopy slides for light microscopy scans. A second x-ray scan was then performed. The mass distribution of calcification was measured in both conditions as described above.

2.2 | X-ray microtomosynthesis parameters and reconstruction of z-stacks

The microscope is shown in Figure 1. Commercially available x-ray source, detector and sample stage were integrated into a custom-built frame. The sample stage was motorised in the horizontal *xy* plane under computer control. It was scanned linearly across the x-ray cone beam. Referring to Figure 1, the key of straight-line microtomosynthesis is that the x-ray cone beam spans a wide angle, in this case an angle of 85° . During the scan, as the sample traverses the wide cone beam, each point in the sample receives rays from continually changing directions, which span 85° . In effect, it is equivalent to rotating the sample over a range of angle equal to the span of the cone beam.

The field of view in the direction along the scan was set by the travel range of the scan, which was extended for long samples. The x-ray tube had a focal spot of $5 \mu\text{m}$ at the operating condition of 30 kV/160 μA . The minimum sample-to-focal spot distance was 7.5 mm, corresponding to a 16.8 \times geometric magnification. The flat panel x-ray area detector was designed for clinical mammography and had a pixel size of $74.8 \mu\text{m}$. Each projection image had 3072×3840 pixels. During the scan, projection images were acquired continuously at a frame rate of 6.9 frames/second. Up to 6250 projections were acquired at a total scan time of 5-15 minutes. Image data were continually saved into a fast, solid-state hard disk in the instrument-control computer from the memory buffer of the x-ray detector. The scan direction of the sample stage (*x* or *y*), the travel range and the speed of the scan movement were set as appropriate for the

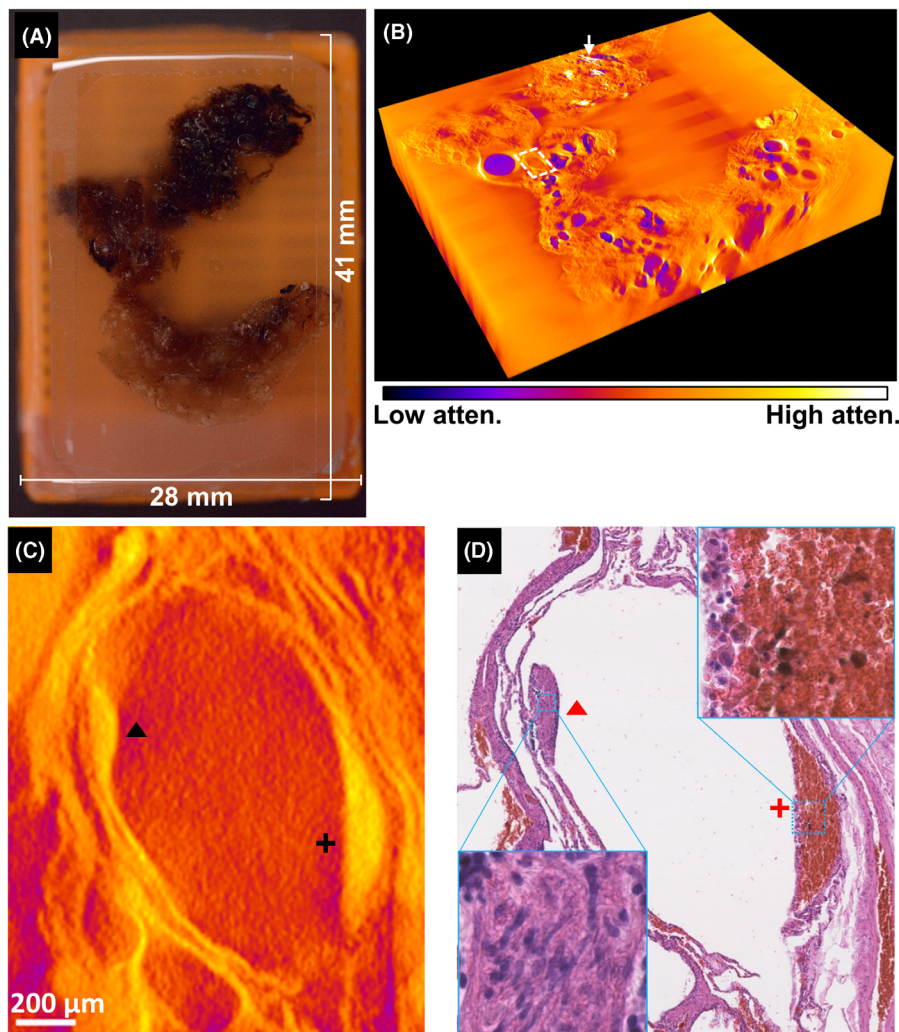


FIGURE 3 X-ray tomosynthesis scan and histology of the lung parenchyma specimen from a patient with the cystic lung disease lymphangioleiomyomatosis (LAM). (A) A photo of the paraffin block containing the specimen. (B) Part of the reconstructed 3D volume from microtomosynthesis, with the top surface at 1.76 mm below the surface of the paraffin block. The top surface cuts across several LAM cysts, one of which is highlighted by the dotted rectangle. The white arrow points to aggregates of macrophages containing cellular debris which appear hyper intense. The blue circular areas of very low attenuation are air pockets in the paraffin. (C) In a magnified view of the cyst outlined by the dotted rectangle in panel B, two sections of the cyst wall appear thickened, indicated by the black triangle and cross markers. (D) Histological image of a thin section at the same location with haematoxylin and eosin staining, with the thickened wall segments marked by the red triangle and cross. The thickened sections were recognised as a nodule consisting of smooth muscle cells (red triangle), and a sedimentation of erythrocytes (red cross). The insets are magnified views of the interior of the thickened sections, outlined by blue dotted rectangles

orientation of the sample, the size of the area to be imaged, and the need to limit the scan to within 15 minutes. The practical scan range was between 15 and 75 mm depending on the sample size, corresponding to a scan speed of up to 83.3 μm/s. An in-house software written in Labview and C was used to synchronously control the operation of the x-ray detector and the movement of the sample stage. The user set the relevant parameters in the software prior to starting the scan, including the image acquisition rate, the scan direction, the starting coordinates of the sample stage, the scan speed and range.

Image reconstruction employed a standard filtered back-projection procedure: the projection intensities were converted to attenuation images relative to blank refer-

ence shots, and prefiltered; To reconstruct a cross-sectional slice, the projection images were shifted laterally by the appropriate amount such that points in that cross-section were aligned; the shifted projection images were summed with the appropriate weighting and normalisation to provide the cross-sectional image. This procedure provides a stack of depth-resolved cross-sectional images of the sample, called a z-stack. A z-stack contained up to 3000 slices of 5-7 μm intervals to cover the whole thickness of the sample. A filtered back-projection algorithm was used for reconstruction²³ with modifications to reduce truncation artefacts. The z-stack had sufficient depth resolution to allow partial 3D visualisation and curved digital cross-sections to follow anatomical features.

2.3 | Characterisation of system resolution and modulation transfer function

As is inherent with tomosynthesis, the images contained out-of-plane shadows due to the limited range of the view angles. The extent of the shadows and the system resolution were quantified by measurements of the line spread function and the modulation transfer function, using a 5 μm tungsten wire target. Referring to Figure 1, the wire was laid horizontally on the sample stage along the y direction, at 9 mm vertical distance from the x-ray source focal spot, corresponding to $14\times$ geometric magnification. The stage was scanned in the x direction. The z -stack of images were reconstructed at 1.5 μm in-plane pixel size and 1.5 μm slice spacing.

2.4 | Benchmark scans on two commercial micro-CT scanners

The two systems were the Skyscan 1172 system and its successor the 1272 system (Bruker, Billerica, MA, USA). Due to detector and beam size constraints of the systems, the sample-to-focal spot distance was >10 cm to cover the 2.5 cm FFPE blocks (Figure 2A) in the field of view. On the Skyscan 1172 system, the optimal parameters for a 3-hour scan were determined through trials. The scan parameters were x-ray tube setting of 29 kV/167 μA (4.8 W), camera matrix of 3000 by 2096, sample rotation step of 0.20° , 1019 projections over 203.70° rotation angle, 1.767-second exposure per shot, average over 5 exposures per angle and total scan time of 3.0 hours. Reconstructed image voxel size was $30.5 \times 30.5 \times 60.9 \mu\text{m}^3$.

On the Skyscan 1272 system, the optimal parameters for a 3-hour scan were determined by a tuning procedure provided by the manufacturer. The scan parameters were x-ray tube setting of 70 kV/142 μA (9.9 W), camera matrix of 2452 by 1640 after 2×2 binning, sample rotation step of 0.20° , 939 projection angles over 187.8° rotation angle, 1.7-second exposure per shot, average over 5 exposures per angle, and total scan time of 2 hours 46 minutes. Reconstructed image voxel size was $10.7 \times 10.7 \times 32.1 \mu\text{m}^3$.

3 | RESULTS

In all tissue samples, microtomosynthesis provided tissue structures at the 5–10 μm scale, and fulfilled its purpose of finding regions of interests for subsequent sectioning and histopathology procedures, or providing independent information that complement classic histopathology. The results from the representative examples listed in the ‘Materials and Methods’ section above are described

below in separate subsections, with detailed information included in figure legends. As mentioned previously, they presented a range of soft tissue contrast from strong to weak, depending on the type of sample and its state of preparation.

3.1 | Example of coronary artery samples from an HIV patient donor

Figure 2(B) illustrates a cross-section through the reconstructed 3D volume of the paraffin block, and Figure 2(C) a cross-section at the same depth from the benchmark micro-CT scan on the Skyscan 1172 system, which verified the location of the microtomosynthesis cross-section. The contrast-to-noise ratio (CNR) between the vessel wall and the surrounding wax medium was measured. It was 14.64 ± 2.47 at a voxel size of 7 μm for the tomosynthesis scanner. The benchmark scan was reconstructed at a voxel size of $30.5 \times 30.5 \times 60.9 \mu\text{m}^3$, which had sufficient tissue visibility to verify the z -stack of images from the tomosynthesis scan. The second benchmark scan on the Skyscan 1272 system provided a smaller reconstruction voxel size but lower tissue visibility.

One of the coronary artery segments is magnified in Figure 2(D). A new finding was the isolated bright dots at the boundary of the intima and media layers of the vessel wall, indicating microcalcification deposits of 10–20 μm size (arrows in Figure 2D). As detailed in Ref. (18), these were matched to dark spots by von Kossa stain in histology sections (Figure 2E), which indicated calcium phosphate deposits. The histology images showed that the calcification was in the internal elastic lamina (IEL) layer (Figure 2E). Their presence in the intact tissue by x-ray ruled out particle contaminants that may be introduced in the sectioning procedure. The calcification was recognised as the initiation of Mönckeberg medial calcific sclerosis, as part of the vascular disease associated with HIV in this patient.¹⁹

3.2 | Example of lung parenchymal tissue specimen from a LAM patient

These samples presented less contrast than the paraffin-embedded arteries described above (Figure 3). Lung parenchyma appeared thinly dispersed in the paraffin block, as the density of parenchyma is 13% of solid tissue.²⁴ Furthermore, instead of solid tumours, which would contrast well with parenchyma, our target was the thin wall surrounding an area of missing parenchyma. Figure 3(B) illustrates part of the reconstructed 3D volume from microtomosynthesis. The exposed top surface is at a level of 1.76 mm below the surface of the block, and cuts across several

LAM cysts. One of the cysts is magnified in Figure 3(C). The wall of the cyst contained two thickened segments. A histology image of the exact location with H&E staining is shown in Figure 3(D), which provided an exact match of soft tissue structures with the tomosynthesis image of Figure 3(C). The thickened sections of the cyst wall are further magnified and shown in the insets in Figure 3(D). By the morphology of the cells, they were recognised as a nodule consisting of smooth muscle cells, and a sedimentation of erythrocytes. In clinical ultra-high resolution CT scans of LAM patients, cyst walls are seen with similar appearance to these images, although at lower levels of resolution.^{25,26}

3.3 | Example of ApoE^{-/-} mouse heart specimen

Figure 4(A) illustrates a cross-section through the reconstructed 3D volume, at a level of 2.07 mm below the surface of the paraffin block. The section bisects the aortic root which was 1.33 mm in diameter. Visible soft tissue structures were the main chambers of the heart, walls of major blood vessels including the aorta and main coronary arteries, aortic valve leaflets and some myocardial fibre structures. Calcification deposits were seen in the aortic wall and in the hinge of a valve leaflet. The mass density of calcification is represented in colour scale in a magnified image of the aortic root (Figure 4B). Figure 4(C) illustrates the 3D disposition of the calcification deposits in a partial 3D rendition of the subvolume containing the aortic root. The total mass of calcification was 0.42 μg . A movie of a 360° rotation of the 3D render is available as a Supplemental Video. The 3D rendition was partial due to the incomplete coverage of projection angles in tomosynthesis.

3.4 | Example of a Eln^{+/-} mouse brain specimen

The reconstructed 3D volume of the paraffin block is illustrated in Figure 5(A). The scan revealed an unusual feature of the basilar artery at the base of the brain (Figure 5B), which is visible in a digital cross-section that bisects the vessel lumen along its length (Figure 5C). The basilar artery appeared to be split at mid length into two parallel vessels in the anterior portion of the artery. The appearance was explained by a transverse cross-sectional image of the vessel lumen at the anterior portion (Figure 5D). The vessel wall folded inward to form a 'V'-shaped lumen. As a result, the longitudinal cross-section cut across the two arms of the 'V', giving the appearance of a bifurcation of the basilar artery.

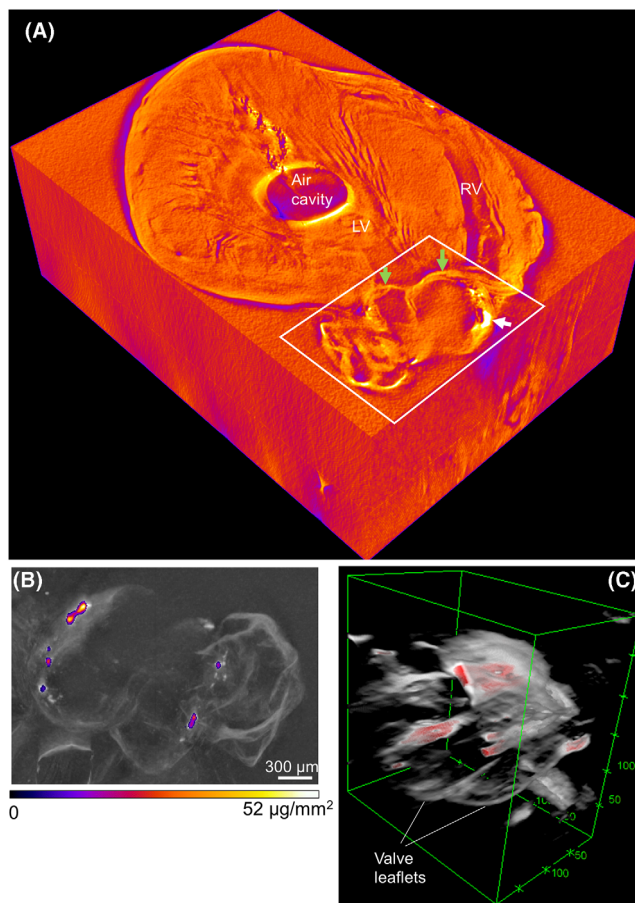


FIGURE 4 X-ray tomosynthesis scan of a paraffin block containing an unstained heart specimen from an ApoE^{-/-} mouse. (A) A cross-section through the re-constructed 3D volume that bisects the left ventricle (LV) and the right ventricle (RV). The section is at 2.07 mm below the surface of the block, and cuts through the aortic root (outlined by the white rectangle). Green arrows point to the leaflets of the aortic valve. Calcification deposits in the aortic wall appear hyper bright, as indicated by the white arrow. (B) A magnified top-down view of the aortic root area outlined in panel A. The greyscale represents x-ray attenuation, and the mass density of calcification is represented in colour scale. Calcification deposits were seen in the aortic wall and the hinge of a valve leaflet. (C) A partial 3D rendition of the subvolume containing the aortic root illustrates the 3D positions of the calcification deposits in red colour. The total mass of calcification was 0.42 μg . A movie of a 360° rotation of the 3D render is available as a Supplemental Video. The 3D rendition was partial due to the incomplete coverage of projection angles in tomosynthesis

3.5 | Example of a ApoE^{-/-} mouse aorta specimen

The fresh aorta sample in distilled water (Figure 6A) presented weaker tissue contrast when compared to the paraffin-embedded samples above. A digital cross-section

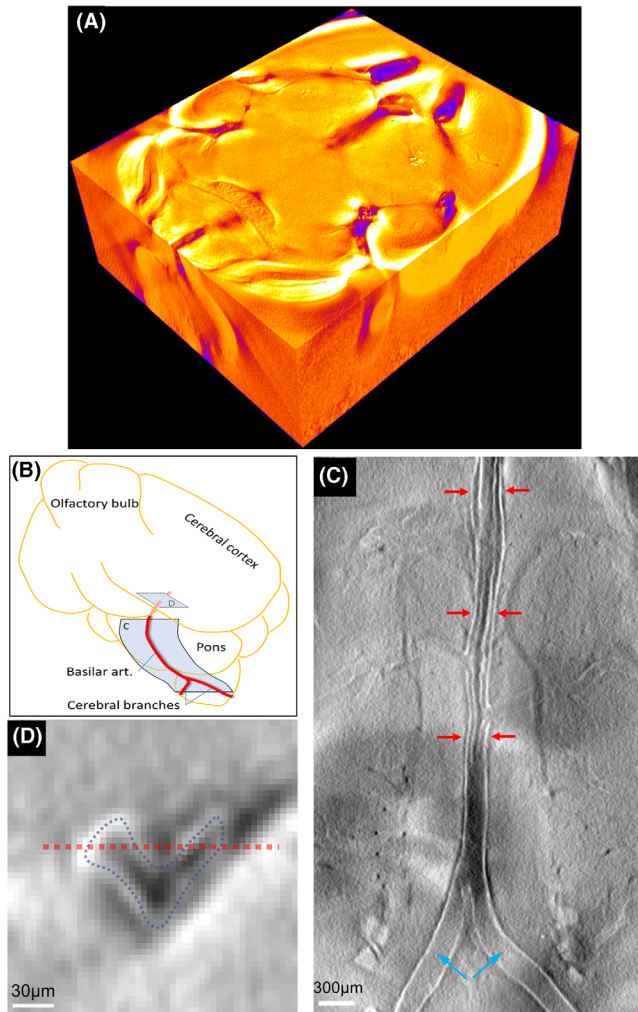


FIGURE 5 X-ray tomosynthesis scan of a paraffin block containing an unstained brain sample from a Eln +/- mouse. **(A)** A cut-away of the reconstructed 3D volume showing the degree of visibility of brain structures. The top surface is at 2.84 mm below the surface of the paraffin block. Blue regions are low density areas, including ventricles and gaps between solid tissue. **(B)** A sketch showing the location of the basilar artery on the underside of a mouse brain. The basilar artery branches into the two cerebral arteries in the posterior, and curves upward into the mid brain at the front. The blue surfaces marked 'C' and 'D' are the location of digital cross-sections described below. **(C)** A digital cross-section was reconstructed from the 3D volume to follow the course of the basilar artery (the blue surface marked 'C' in the sketch in panel B). Greyscale represents x-ray attenuation. Vessel walls appear as bright lines due to their higher density than surrounding tissue. The basilar artery appears to split at mid length into two parallel vessels in the anterior portion of the artery (red arrows). The two cerebral arteries are indicated by cyan arrows. **(D)** A transverse cross-sectional image of the anterior portion of the basilar artery, along the blue plane marked 'D' in the sketch in panel B. It shows that the vessel wall has folded inward to form a 'V'-shaped lumen (dotted blue line). As a result, the longitudinal cross section (dotted red line) cuts across the two arms of the 'V', giving the appearance of a split basilar artery in the image in panel C

that bisects the lumen along its length was reconstructed from a z-stack of 600 cross-sectional images (Figure 6B). A mid-section of the aorta is magnified and shown in Figure 6(C). Here, the visible soft tissue structures were the vessel wall, atherosclerotic plaques in the lumen, and perivascular fat. In the aortic arch, calcification appears as hyper intense areas, extending down into the beginning of the descending segment, and up into the roots of the ascending vessel branches. A magnified view of the aortic arch is shown in Figure 6(D), where the mass density of calcification is overlaid in colour-scale. The total amount of calcification based on x-ray attenuation was 251 μg .

After the aorta was dissected open, stained and sealed in a slide chamber (Figure 6E), light microscopy showed pink/red staining of the yellow fatty plaques on the surface of the lumen (Figure 6F). A matching x-ray image was made by averaging a subset of the tomosynthesis z-stack (Figure 6G). Areas of low x-ray attenuation were matched to the red-stained areas in the light microscopy image of Figure 6(F). Calcification was all concentrated in the aortic arch, and overlapped with red-stained plaques in Figure 6(F). The amount of calcification was 46 μg by x-ray attenuation. This was 18% of the amount in the intact sample in Figure 6(D). Therefore, some of the calcification fragments were likely washed away in the dissection and slide preparation.

3.6 | System resolution and modulation transfer function

The results are summarised in Figure 7. An image of the line spread function (LSF) across the 5 μm tungsten wire target in the x-z plane is shown in the inset. Modulation transfer functions (MTF) in the scan(x) and z-depth directions were obtained from Fourier transformation of the x and z cross-section profiles of the LSF. The measured 10% contrast resolution in the scan and z-depth directions were 7.3 μm (half-period of 68.5 line pairs/mm) and 22.0 μm (half-period of 22.8 line pairs/mm), respectively. The tilt of the LSF profile was due to variation in the effective size of the x-ray focal spot over the duration of the scan.

The thickness of the sample can be a significant influence on the MTF, when the source-to-image distance at the backside of the sample is large enough such that the geometric magnification factor drops below the level where the detector resolution becomes a limiting factor for the MTF. The FFPE blocks we have scanned were typically 5 mm thick, covering a 7.5-12.5 mm distance from the source. The corresponding geometric magnification factor ranged from 16.8 to 10.1. The effective pixel size of the detector at the image plane ranged from 4.45 to 7.42 μm , corresponding to a spatial frequency range of 112-67.4 lp/mm,

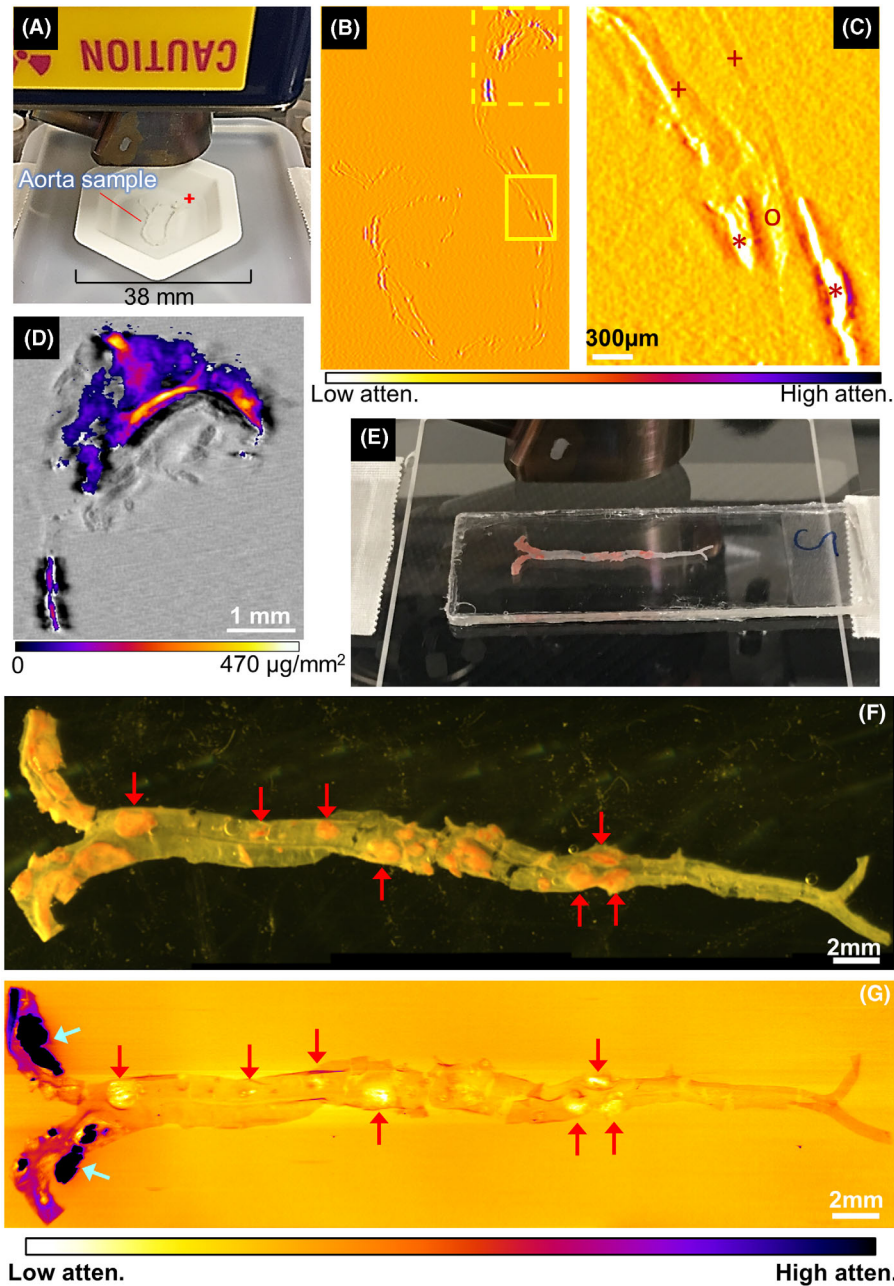


FIGURE 6 Tomosynthesis scans and measurement of the total mass of calcification in the aorta sample of an ApoE^{-/-} mouse before and after processing. **(A)** A photo of the fresh aorta sample in distilled water in a weigh boat on the scanner stage. The aortic arch is marked by the red '+'. The common iliac branches at the other end of the aorta are also visible. **(B)** The fresh aorta presented weak soft tissue contrast when immersed in water. A digital dissection along the length of the aorta was reconstructed from the z-stack of 600 cross-sectional images. The aortic arch region is outlined with the yellow dotted rectangle. Calcification appears as black/blue streaks of ultra-high x-ray attenuation. A mid-section of the descending aorta is marked by the solid rectangle and further magnified below. **(C)** A magnified view of a mid-section of the aorta outlined by the solid rectangle in panel B. The vessel walls, marked by '+', are weakly visible by their slightly higher x-ray attenuation relative to water, while an atherosclerotic plaque in the lumen (marked by 'o') and perivascular fat (marked by '*') are visible as bright areas of lower x-ray attenuation. The wavy background is a shadow artefact from particles in the material of the weigh boat. **(D)** A magnified image of the aortic arch outlined by the yellow dotted rectangle in panel B. The greyscale represents x-ray attenuation, and the colour overlay represents the areal density of calcification in a colour scale. The total mass of calcification was 251 μg in the fresh sample. **(E)** A photo of the dissected aorta sample stained with Sudan IV red for lipids, and sealed in a buffer solution in a slide chamber. **(F)** Light microscopy image of the sample showed pink/red staining of the fatty plaques on the surface of the lumen. **(G)** A z-stack average showed areas of low x-ray attenuation that were matched to the red-stained areas of the photo, as indicated by red arrows. Calcification was concentrated in the aortic arch as indicated by cyan arrows, and overlapped plaque areas that were stained red in panel F. The total mass of calcification by x-ray attenuation was 46 μg in the dissected sample

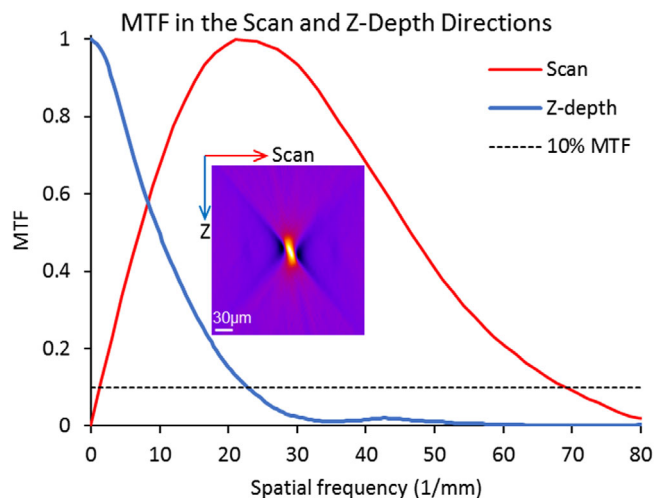


FIGURE 7 Measurement of the line spread and modulation transfer function of the microtomosynthesis scanner. A tungsten wire of $5\ \mu\text{m}$ diameter was the target. Referring to Figure 1, the wire was laid horizontally on the sample stage along the y direction, at $9\ \text{mm}$ vertical distance from the x-ray source focal spot, corresponding to $14\times$ geometric magnification. The stage was scanned in the x direction. The z -stack of images were reconstructed at $1.5\ \mu\text{m}$ in-plane pixel size and $1.5\ \mu\text{m}$ slice spacing. A cross-sectional image of the line spread function (LSF) across the wire is shown in the inset. The tilt of the LSF profile was due to variation in the effective size of the x-ray focal spot over the duration of the scan. Modulation transfer functions (MTF) in the x and z -depth directions were obtained from Fourier transformation of the x and z cross-section profiles of the LSF. These are plotted. The 10% level of relative contrast is marked by the dotted line. The measured 10% contrast resolution in the scan and z -depth directions were $7.3\ \mu\text{m}$ (half-period of 68.5 line pairs/mm) and $22.0\ \mu\text{m}$ (half-period of 22.8 line pairs/mm), respectively

relative to the MTF width of $68.5\ \text{lp/mm}$ (10% contrast) at the source-to-image distance of $9\ \text{mm}$. Thus, geometric magnification factors below 10, or sample-to-image distances beyond $12.6\ \text{mm}$, will appreciably broaden the MTF.

Fortunately, the procedure to make standard FFPE blocks ensures that the tissue is always at the very top of the block, in order to facilitate sectioning (pouring warm wax over a tissue sample placed at the bottom of an inverted mould). This also minimises the distance between the x-ray source and the tissue sample within the wax block for the scan.

The extent of the LSF in the Z direction represented the extent of the out-of-plane shadow artefact, which in filtered back-projection is primarily cast by high spatial-frequency features within the x - y plane, such as the sharp edges of a uniform high-contrast object (ie a metal disk), due to the high-pass nature of the filtering step in the reconstruction algorithm. For example, with an extended object in the x - y plane, the shadow at a given z offset is the convolution of the LSF profile at that z offset with the pro-

file of the object in the x - y plane. Thus, due to the oscillatory profile of the LSF in the x - y plane, the shadow primarily emanates from areas of sharp gradients in the object, such as the edges.

4 | CONCLUSION

In this study, we explored straight-line microtomosynthesis of unstained tissue samples in either aqueous or paraffin-embedded state for guiding subsequent pathology procedures. The main advantage of this mode of scanning is that with the same hardware components, it allowed flat samples, such as tissue in standard paraffin-embedding cassettes and in flat dishes, to be kept as close as possible to the x-ray focal spot. This then maximised the photon flux density through the sample, and also the geometric magnification factor. Both contributed to the resolution and contrast-to-noise ratio of the resulting images. In a variety of unstained human and animal tissue samples, the scanner provided $7.3\ \mu\text{m}$ resolution (10% contrast, half-period of 68.5 line pairs/mm) in z -stacks of 5 - $7\ \mu\text{m}$ slice intervals, with scan times of 5 - 15 minutes. Microtomosynthesis provided detailed tissue structures at varying levels of contrast depending on the type and state of the sample. The z -stacks proved useful in locating the depth and position of interesting features for subsequent sectioning and histopathology analysis.

The tradeoff of this mode relative to micro-CT was the lack of complete 3D information, which meant that 3D rendering was only partial, and the resolution in depth was less than in the lateral plane. Despite the tradeoff, we found in practice that the limiting factor with unstained samples in a limited time window was often the visibility of tissue structures, which was helped by the contrast-to-noise ratio of the method. Beyond the weighted filtered back-projection algorithm for image reconstruction, more advanced algorithms, such as constrained optimisation¹⁴ and algebraic iterative reconstruction¹⁸ have been shown to substantially reduce the typical out-of-plane shadow artefacts of tomosynthesis, although computation time can be a limiting factor at the moment. It should be noted that when imaging time or sample stability are not limited, the full CT scan, with its complete 3D information, is more suitable than tomosynthesis for detailed studies.

Straight-line tomosynthesis is currently used in security screening of luggages.¹⁷ It is conceivable that a similar operation can be developed to scan a continuous stream of standard FFPE blocks on indexed carriers on a conveyor belt, particularly in combination with automated sectioning systems.²⁷ This level of automation may help to streamline the workflow in centralised pathology test centres.²⁸

ORCID

Christopher K. E. Bleck  <https://orcid.org/0000-0003-1029-3444>

Han Wen  <https://orcid.org/0000-0001-6844-2997>

REFERENCES

- Cserni, G., Amendoeira, I., Apostolikas, N., Bellocq, J. P., Bianchi, S., Boecker, W., ... Wells, C. A. (2004). Discrepancies in current practice of pathological evaluation of sentinel lymph nodes in breast cancer. Results of a questionnaire based survey by the European Working Group for Breast Screening Pathology. *Journal of Clinical Pathology*, *57*, 695–701
- Weaver, D. L., Le, U. P., Dupuis, S. L., Weaver, K. A. E., Harlow, S. P., Ashikaga, T., & Krag, D. N. (2009). Metastasis detection in sentinel lymph nodes: Comparison of a limited widely spaced (NSABP Protocol B-32) and a comprehensive narrowly spaced paraffin block sectioning strategy. *American Journal of Surgical Pathology*, *33*, 1583–1589
- Kumaraswamy, V., & Carder, P. J. (2007). Examination of breast needle core biopsy specimens performed for screen-detected microcalcification. *Journal of Clinical Pathology*, *60*, 681–684
- Albers, J., Pacile, S., Markus, M. A., Wiart, M., Velde, G. V., Tromba, G., & Dullin, C. (2018). X-ray-based 3D virtual histology – Adding the next dimension to histological analysis. *Molecular Imaging and Biology*, *20*, 732–741
- du Plessis, A., Broeckhoven, C., Guelpa, A., & le Roux, S. G. (2017). Laboratory x-ray micro-computed tomography: A user guideline for biological samples. *Gigascience*, *6*, 1–11. <https://doi.org/10.1093/gigascience/gix027>
- Stock, S. R. (2019). *MicroComputed tomography: Methodology and applications*, 2nd edn. Boca Raton, FL: CRC Press
- Laperle, C. M., Hamilton, T. J., Wintermeyer, P., Walker, E., Shi, D. X., Anastasio, M. A., ... Rose-Petrucci, C. (2008). Low density contrast agents for x-ray phase contrast imaging: The use of ambient air for x-ray angiography of excised murine liver tissue. *Physics in Medicine and Biology*, *53*, 6911–6923
- Dudak, J., Zemlicka, J., Karch, J., Patzelt, M., Mrzilkova, J., Zach, P., ... Krejci, F. (2016). High-contrast X-ray micro-radiography and micro-CT of ex-vivo soft tissue murine organs utilizing ethanol fixation and large area photon-counting detector. *Scientific Reports*, *6*, 30385
- Morales, A. G., Stempinski, E. S., Xiao, X., Patel, A., Panna, A., Olivier, K. N., ... Wen, H. (2016). Micro-CT scouting for transmission electron microscopy of human tissue specimens. *Journal of Microscopy*, *263*, 113–117
- Dudak, J., Zemlicka, J., Krejci, F., Karch, J., Patzelt, M., Zach, P., ... Mrzilkova, J. (2016). Evaluation of sample holders designed for long-lasting X-ray micro-tomographic scans of ex-vivo soft tissue samples. *Journal of Instrumentation*, *11*, C03005
- Dobbins, J. T., & Godfrey, D. J. (2003). Digital x-ray tomosynthesis: Current state of the art and clinical potential. *Physics in Medicine and Biology*, *48*, R65–R106
- Zhou, J., Maisl, M., Reiter, H., & Arnold, W. (1996). Computed laminography for materials testing. *Applied Physics Letters*, *68*, 3500–3502
- Gondrom, S., Zhou, J., Maisl, M., Reiter, H., Kröning, M., & Arnold, W. (1999). X-ray computed laminography: An approach of computed tomography for applications with limited access. *Nuclear Engineering and Design*, *190*, 141–147
- Gao, H., Zhang, L., Chen, Z., Xing, Y., Xue, H., & Cheng, J. (2013). Straight-line-trajectory-based X-ray tomographic imaging for security inspections: System design, image reconstruction and preliminary results. *IEEE Transactions on Nuclear Science*, *60*, 3955–3968
- O'Brien, N. S., Boardman, R. P., Sinclair, I., & Blumensath, T. (2016). Recent advances in X-ray cone-beam computed laminography. *Journal of X-Ray Science and Technology*, *24*, 691–707
- Ziedses des Plantes, B. G. (1932). Eine Neue Methode Zur Differenzierung In Der Röntgenographie (PLANIGRAPHIE). *Acta Radiologica os-13*, 182–192
- US Department of Homeland Security (2018). *Advanced integrated passenger and baggage screening technologies*. Retrieved from <https://www.dhs.gov/sites/default/files/publications/TSA%20-%20Advanced%20Integrated%20Passenger%20Screening%20Technologies.pdf>
- Sechopoulos, I. (2013). A review of breast tomosynthesis. Part II. Image reconstruction, processing and analysis, and advanced applications. *Medical Physics*, *40*, 014302
- Wen, H., Martinez, A. M., Miao, H. X., Larsen, T. C., Nguyen, C. P., Bennett, E. E., ... Gharib, A. M. (2018). Correlative detection of isolated single and multi-cellular calcifications in the internal elastic lamina of human coronary artery samples. *Scientific Reports*, *8*, 10978
- Taveira-DaSilva, A. M., & Moss, J. (2015). Clinical features, epidemiology, and therapy of lymphangioleiomyomatosis. *Clinical Epidemiology*, *7*, 249–257
- Cameron, J. R., Mazess, R. B., & Sorenson, J. A. (1968). Precision and accuracy of bone mineral determination by direct photon absorptiometry. *Investigative Radiology*, *3*, 141–150
- Li, D. Y., Faury, G., Taylor, D. G., Davis, E. C., Boyle, W. A., Mecham, R. P., ... Keating, M. T. (1998). Novel arterial pathology in mice and humans hemizygous for elastin. *Journal of Clinical Investigation*, *102*, 1783–1787
- Gao, H., Zhang, L., Chen, Z., Xing, Y., Cheng, J., & Qi, Z. (2007). Direct filtered-backprojection-type reconstruction from a straight-line trajectory. *Optical Engineering*, *46*, 057003
- Karimi, R., Tornling, G., Forsslund, H., Mikko, M., Wheelock, Å. M., Nyrén, S., & Sköld, C. M. (2014). Lung density on high resolution computer tomography (HRCT) reflects degree of inflammation in smokers. *Respiratory Research*, *15*, 23
- Larsen, T. C., Gopalakrishnan, V., Yao, J. H., Nguyen, C. P., Moss, J., & Wen, H. (2018). Optimization of a Secondary VOI Scan for Lung Imaging in a Clinical CT Scanner. *Journal of Applied Clinical Medical Physics*, *19*, 271–280

26. Larsen, T. C., Hasani, A. M., Rollison, S. F., Machado, T. R., Jones, A. M., Julien-Williams, P., ... Wen, H. (2020). Clinical CT underestimation of the percentage volume occupied by cysts in patients with lymphangioliomyomatosis. *Clinical Imaging*, *59*, 119–125
27. Onozato, M. L., Hammond, S., Merren, M., & Yagi, Y. (2013). Evaluation of a completely automated tissue-sectioning machine for paraffin blocks. *Journal of Clinical Pathology*, *66*, 151–154
28. Kohl, S. K., Lewis, S. E., Tunnicliffe, J., Lott, R. L., Spencer, L. T., Carson, F. L., ... Brown, R. W. (2011). The College of American Pathologists and National Society for Histotechnology Workload Study. *Archives of Pathology & Laboratory Medicine*, *135*, 728–736

SUPPORTING INFORMATION

Additional supporting information may be found online in the Supporting Information section at the end of the article.

How to cite this article: Nguyen DT, Larsen TC, Wang M, et al. X-ray microtomosynthesis of unstained pathology tissue samples. *Journal of Microscopy*. 2021;283:9–20.
<https://doi.org/10.1111/jmi.13003>